

**UNIVERSITY OF TWENTE**  
FACULTY OF SCIENCE & TECHNOLOGY  
MAGNETIC DETECTION AND IMAGING

## **A dynamic heart phantom based on Polyvinyl Alcohol Cryogel for Temperature Validation after Radiofrequency Ablation**

Shanne Doest  
s2591006

**Supervisors:**

prof.dr.ir. B. ten Haken (Bernard)  
dr. ir. W.M. Brink (Wyger)  
dr. ir. L. Fresiello Meng (Libera)

BSc Thesis Biomedical Technology  
09-11-2023

---

## **Abstract**

### **Background**

Atrial fibrillation is the most common type of cardiac arrhythmias, which can lead to irregular heart rhythms. A new advancement in the treatment is radio-frequency ablation (RFA). This treatment involves applying a radiofrequency energy to create controlled tissue damage. Post-ablation assessment of the temperature changes is possible through  $T_1$  and  $T_2$  mapping. Besides that, real-time MR thermometry is a promising technique for the guidance of the procedure.

The development of a phantom is necessary to simulate the heart's dielectric properties for effective RFA training and validation. In this study, a phantom composed of the temperature sensitive material polyvinyl alcohol (PVA) has been developed.

### **Methods**

To study the relationship between temperature and  $T_1/T_2$  relaxation times, 33 spherical phantoms were heated in a water bath to different temperatures. A rectangular phantom was used to perform needle ablation from which 3D  $T_1/T_2$  maps could be obtained and converted into temperature maps. Two final cardiac phantoms underwent radiofrequency catheter ablation and were also evaluated using 3D  $T_1/T_2$  maps, from which the temperature maps could be generated. All imaging was done on a Siemens 1.5T MRI scanner with specific scanning protocols for  $T_1$  and  $T_2$  mapping.

### **Results**

A positive, and linear correlation has been established between elevated temperatures and the increase in  $T_1$  relaxation times. This linear relationship with temperature does not entirely apply for  $T_2$  relaxation times. The ablated areas can be visualized, but not yet validated correctly, by deriving temperature maps from the  $T_1$  and  $T_2$  maps.

### **Conclusion**

A dynamic heart phantom composed of PVA and salt has the potential for validation and training in RFA procedures, serving as a basis for the development of monitoring techniques.

---

## Samenvatting

### Achtergrond

Atriale fibrillatie, de meest voorkomende hartritmestoornis, kan leiden tot een onregelmatig hartritme. De behandeling hiervan is uitgebreid met radiofrequente ablatie (RFA). Hierbij wordt radiofrequente energie gebruikt om gecontroleerde weefselschade te veroorzaken. Het onderzoeken van temperatuur veranderingen is mogelijk door post-ablatie  $T_1$  and  $T_2$  mappen te genereren en om te zetten in temperatuurkaarten. Daarnaast is MR thermometrie een veelbelovende techniek voor het begeleiden van de procedure.

Het ontwikkelen van een fantoom is noodzakelijk voor het nabootsen van de di-elektrische eigenschappen van het hart voor effectieve RFA training en validatie. In deze studie is onderzoek gedaan naar een fantoom gemaakt van het temperatuur sensitieve polyvinyl alcohol (PVA).

### Methode

Om de relatie tussen temperatuur en  $T_1/T_2$  te onderzoeken, werden 33 sferische fantomen verwarmd in een waterbad tot verschillende temperaturen. Naaldablatie werd uitgevoerd op een rechthoekig fantoom, waarvan 3D  $T_1/T_2$  mapping werd gebruikt om de temperatuurkaarten te generen. Twee hart fantomen werden gebruikt voor de radiofrequente katheterablatie en geëvalueerd aan de hand van 3D  $T_1/T_2$  mapping die werden geconverteerd naar temperatuurkaarten.

### Resultaten

Uit het onderzoek is gebleken dat er een positieve, lineaire relatie bestaat tussen de  $T_1$  relaxatietijd en temperatuur. Deze lineaire relatie met temperatuur geldt niet voor de  $T_2$  relaxatie tijden. De ge-ableerde gebieden kunnen worden gevisualiseerd, maar nog niet worden gevalideerd, door  $T_1$  en  $T_2$  mappen om te zetten in temperatuurkaarten.

### Conclusie

Een dynamisch hartfantoom gemaakt van PVA en zout kan potentieel worden gebruikt voor de valiatie en training van RFA procedures en als basis voor het ontwikkelen van monitoring technieken.

## Contents

<b>1</b>	<b>Introduction</b>	<b>6</b>
1.1	Arrhythmia . . . . .	6
1.2	Radiofrequency catheter ablation . . . . .	6
1.3	Temperature assessment . . . . .	7
1.3.1	$T_1$ and $T_2$ mapping . . . . .	7
1.3.2	Real-time MR thermometry . . . . .	7
1.4	Different methods to test the RFA technique . . . . .	7
1.5	Phantoms: state of art . . . . .	8
1.6	Polyvinyl alcohol . . . . .	8
1.7	Dielectric properties of the human heart . . . . .	9
1.8	Aim . . . . .	10
<b>2</b>	<b>Methods</b>	<b>10</b>
2.1	Fabrication protocol . . . . .	10
2.2	3D ventricle mold design . . . . .	10
2.3	Temperature calibration and MRI-based $T_1$ & $T_2$ relaxation . . . . .	11
2.4	Needle ablation of a rectangular phantom . . . . .	11
2.5	Radiofrequency catheter ablation of the heart phantom . . . . .	12
2.6	Scanning protocol . . . . .	12
2.6.1	$T_1$ and $T_2$ mapping . . . . .	12
2.6.2	Temperature mapping . . . . .	13
<b>3</b>	<b>Results</b>	<b>13</b>
3.1	Temperature calibration with MRI-based $T_1$ and $T_2$ relaxation . . . . .	13
3.2	Needle ablation of a rectangular phantom . . . . .	15
3.2.1	$T_1$ and $T_2$ 3D maps after needle ablation . . . . .	15
3.2.2	Temperature maps after needle ablation . . . . .	17
3.3	Catheter ablation of the heart phantom . . . . .	17
3.3.1	3D $T_1$ and $T_2$ maps after RFA . . . . .	17
3.3.2	Temperature maps after RFA . . . . .	18
<b>4</b>	<b>Discussion</b>	<b>19</b>
4.1	Fabrication protocol . . . . .	19
4.1.1	Number of F-T cycles . . . . .	19
4.1.2	F-T cycle time . . . . .	19
4.1.3	Different used PVA powder . . . . .	19
4.2	Heating of the phantoms . . . . .	20
4.2.1	Temperature of the phantom spheres . . . . .	20
4.2.2	Melting point . . . . .	20
4.3	$T_1$ and $T_2$ relaxation times vs. temperature . . . . .	20
4.3.1	Calibration of $T_1$ and $T_2$ relaxation times . . . . .	20
4.3.2	Variance in $T_1$ and $T_2$ relaxation times . . . . .	22
4.3.3	Re-usability of the phantom . . . . .	22
4.4	Measurement errors and artefacts . . . . .	23
4.4.1	Systematic error needle ablation . . . . .	23
4.4.2	Material transitions . . . . .	23
4.5	Further research recommendations . . . . .	23
4.5.1	Dissolvable inner mold . . . . .	23
4.5.2	Real-time MRI guidance and MR thermometry . . . . .	23
<b>5</b>	<b>Conclusion</b>	<b>24</b>

**References**

**25**

---

## List of abbreviations

**AF** - Atrial fibrillation  
**CT** - Computed Tomography  
**ECG** - Electrocardiogram  
**EM** - Electromagnetic  
**FoV** - Field of View  
**FSE** - Fast Spin Echo  
**F-T** - Freezing-thawing  
**GRE** - Gradient Echo  
**IR** - Inversion Recovery  
**MR(I)** - Magnetic Resonance (Imaging)  
**MW** - Molecular Weight  
**PAA** - Polyacrylamide  
**PLA** - Polylactic acid  
**PVA** - Polyvinyl alcohol  
**PVA-C** - Polyvinyl alcohol - cryogel  
**RF** - Radiofrequency  
**RFA** - Radiofrequency ablation  
**ROI** - Region of interest  
**SE** - Spin Echo  
**TE** - Echo time  
**TI** - Inversion time  
**TR** - Repetition time  
**US** - Ultrasound  
**WT%** - Weight Percentage

# 1 Introduction

## 1.1 Arrhythmia

Cardiac arrhythmias are estimated to affect between 1.5% and 5% of the worldwide population, with an increase of 33% in prevalence observed over the last few years. This trend is expected to continue over the next 30 years.[1] However, not everyone suffering from cardiac arrhythmia experiences noticeable symptoms. The most common type of cardiac arrhythmia is atrial fibrillation (AF). AF disrupts the normal heart rhythm, causing the heart to quiver or fibrillate instead of contracting regularly. This irregularity can lead to the heart beating too slowly (<60 beats per minute), known as bradyarrhythmia, or too quickly (>100 beats per minute), known as tachyarrhythmia.[2]

There are medications and other procedures available to manage the irregular heart rate. Untreated arrhythmias can potentially damage the heart, brain, or other vital organs.[3] Besides medication, pacemakers and defibrillator devices have been suggested as treatment options. A promising advancement in the treatment of cardiac arrhythmias is radiofrequency ablation (RFA).[4]

## 1.2 Radiofrequency catheter ablation

RFA is a secure and economically efficient therapeutic approach for distinct cardiac arrhythmias.[4] The radiofrequency (RF) energy is directed from a catheter's tip to a specific area of the heart's inner lining (the endocardium), which is identified during electrophysiological studies.[5] The catheter will be positioned at a specific location and will send RF energy for multiple seconds or minutes.[6] The energy is generated by the alternated high-frequency RF current. For cardiac ablation, this frequency usually ranges between 350 and 500 kHz.[5] This electromagnetic energy causes the rotation of water molecules in cardiac tissue and thus the frictional, Ohmic, heating of the interface between the catheter and the endocardium.[7] This heat creates tiny, controlled damage and causes cell death. The ablation usually occurs at temperatures over 47°C.[8][9] The myocardium experiences permanent damage when heated for various seconds above at least 50°C.[10] To avoid excessive tissue damage, the ablation temperature should not exceed 100°C.[11]

When applying the RF current, the tissue will be heated due to resistive (direct) and conductive (indirect) heating, see Figure 1. Resistive heating occurs when RF energy is applied at the interface of the catheter electrode and myocardium. This type of heating is rapid and closely aligned with the start and stop of RF energy delivery. The passive process of conductive heating dissipates the heat from the core of the ablation lesion deeper into the myocardium. Conductive heating will persist, even after the discontinued RF energy. A shorter ablation duration will lead to less conductive heating and thus a smaller lesion.[12]

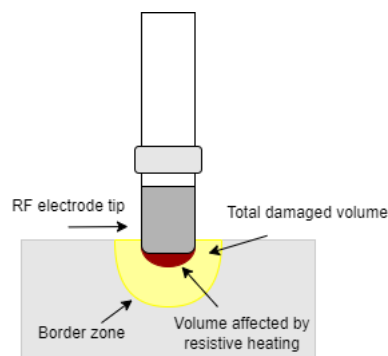


Figure 1: Schematic visualisation of the heated volume. The volume affected by resistive heating is only a small part of the total damaged volume, mainly caused by conductive heating.[12][13]

Mertyna et al.[14] describe a relation between the duration of RF ablation and applied RF current. The specified diameter of coagulation can be achieved with a shorter ablation time by applying a higher current. This also corresponds with the relation between thermal dose and applied current. A higher current relates to a smaller thermal dose. It has appeared, that there is also a relation between the thermal dose and the distance of the

ablated tissue from the RF electrode. If the tissue is further away from the RF electrode, a greater thermal dose is required.[14] To reduce the thermal dose, the catheters tip needs to be placed as close to the tissue as possible and a higher current should be applied.

Until now, it has been a challenge to completely get rid of recurrent AF. The research of Calkins et al.[15] states that within a year after ablation, recurrence happens to 25% to 40% of the patients.[15] To prevent recurrence it is important to accurately guide and monitor the procedure. Currently, X-ray imaging (fluoroscopy) or ultrasound (intracardiac echocardiography) can be used throughout the procedure to see the position of the catheter and verify it is in the right place.[8] However, thermal ablation causes soft tissue changes, which can not be visualized using these techniques. Using MRI would solve this problem. MRI makes it possible to distinguish and characterize differences within the same tissue, and to provide high-resolution images of tissues in 3D.[16][17] Besides that, it is also possible to visualize temperature changes with MR thermometry.[10] Until now, there has been no ethical method available to test the RFA technique and validate temperature changes.

### 1.3 Temperature assessment

#### 1.3.1 $T_1$ and $T_2$ mapping

$T_1$  and  $T_2$  relaxation times are important MRI parameters, especially for tissue characterization.[18] Myocardial tissues, including abnormalities, can be characterized by  $T_1$  and  $T_2$  mapping sequences. These relaxation times can vary with temperature. The  $T_1$  relaxation time quantifies the time hydrogen nuclei take to return to their equilibrium state after being disturbed by an external energy source, such as an RF pulse.  $T_1$  values can vary based on temperature.[19] A linear relationship has been found between  $T_1$  relaxation time and temperature, within a narrow range of temperatures.[18][20] Using this, temperature variations can be detected by  $T_1$  mapping techniques.

The  $T_2$  relaxation time quantifies the time hydrogen nuclei take to lose their coherence and dephase after an RF pulse.[18] In aqueous solutions, an increase in  $T_2$  relaxation time has been observed with rising temperatures.[20] This temperature dependency is less significant, because the  $T_2$  relaxation time is less affected by small temperature changes.[18]

All materials have their own corresponding temperature dependency.[18] With the  $T_1$  and  $T_2$  data, a temperature map can be created to validate temperature changes.

#### 1.3.2 Real-time MR thermometry

A promising technique for the guidance during RFA is cardiac Magnetic Resonance (MR) thermometry. With this technique, temperature changes in the body can be quantitatively measured in real time and changes in soft-tissue contrast can be detected. The guidance is necessary to manage the outcome of the treatment. Real-time MR thermometry can be used to check if the desired lesion is achieved, to detect any potential signs of recurrence or incomplete ablation and to secure the patient's safety regarding immoderate heating.[20][21]

The most common method of MR thermometry is the Proton Resonance Frequency (PRF) shift of water protons. This method makes use of the temperature sensitivity of proton resonance, and depends on the affected resonance frequency induced by the local magnetic field, determined by a shielding constant. Temperature-induced changes in hydrogen bonds affect this shielding in water molecules. A predictable shift in the resonance frequency is caused when water molecules change with temperature. Besides this temperature sensitivity, the PRF shift method offers excellent spatial and temporal resolution. Furthermore, it is not influenced by the type of tissue being treated.[20]

### 1.4 Different methods to test the RFA technique

There are several methods to test and validate RFA equipment and techniques. Starting with in vivo animal studies. This involves testing on or with living animals. Animals have a lot of anatomical and physiological features in common with humans, which makes it a reliable and specific method for testing different techniques.[22] However, there could be differences in results when using animal tissues, instead of human

tissues. It is also important to take the ethical aspect into account. Researchers must follow strict regulations and ethical guidelines. In vivo animal studies are cost intensive and limited to the availability of disease specific animal models. Eventually, these studies need to be tested in human clinical trials.[23]

Another method of testing the RFA technique is on ex vivo tissue models. These models enable studying both physiologic and pathologic (cardiac) function, which makes it more realistic. The results of this study are limited by the lack of systemic interactions and physiological functions, which are present in living organisms.[24]

The most ethical method available is a phantom model. A phantom is an instrument that simulates a part of the human body. It can serve many purposes, such as simulating the properties and characteristics of the human body to test and train specific techniques, to test limitations of specific imaging systems or to calibrate imaging equipment.[25][26] It depends on the main goal of the phantom, which properties are more important than others.

## 1.5 Phantoms: state of art

For the training, monitoring and validation of RFA a phantom should be developed, because it is ethically not desirable to test a specific technique directly on patients. This phantom must mimic the properties and characteristics of the heart and be sensitive to temperature changes. Till this moment, a variety of materials has been used to create phantoms. For example, phantoms made of agar gel. Agar gels are easy and cost-effective to manufacture, possess sufficient mechanical strength, have a high melting point (between 85°C and 95°C), can be easily modified by additional ingredients and can provide tissue-like signal in MRI. Disadvantages of agar gels are the low toughness and fragility. It is also challenging to visualize lesion formation when applying heat.[27]

Gelatin-based phantoms are also relatively easy to make and cost-effective. They can mimic a variety of soft tissues using additional ingredients and can be doped with MRI contrast agents for MRI applications. However, gelatin has a low melting point, which makes it temperature limited. Adding chemical cross-linkers increases the mechanical stiffness and temperature tolerance. This may also lead to unfavorable changes in other parameters.[27]

Phantoms made of silicone are flexible, mechanically strong and resistant to fractures. Silicone is also suitable for the creation of anatomical features. Using silicone makes it possible to simulate ventricular contraction, because of the elasticity silicone maintains. Furthermore, silicone exhibits, in a solid state, stable MR relaxation times. However, silicone is incompatible with organic materials and does not mimic the electromagnetic properties of the heart. Also, the mechanical properties of silicone do not completely match with those of the heart, because of its higher elasticity modulus.[28][29]

Polyacrylamide (PAA) phantoms have a high melting point (between 100°C and 150°C), which makes it suitable for thermal ablation therapies. They can also be doped with MRI contrast agents to modify the MRI properties. The addition of albumin has been investigated as a thermochromic additive. This leads to changes in  $T_2$  relaxation time when it is coagulated, enabling a non-invasive volumetric assessment of the ablation zone.[30] The electrical conductivity of the gel can be adjusted by adding NaCl. The disadvantages of PAA gels are the toxicity of the monomer acrylamide, the limited elasticity and, when containing proteins, the permanent changes when coagulating, which makes them unsuitable for repeated use.[27]

All of these materials are not completely suitable for a dynamic heart phantom to train, monitor and validate RFA. It has been found that Polyvinyl alcohol cryogel (PVA-C) is capable of recording temperature distributions in the range of 45-70°C.[31] As cardiac ablation occurs at temperatures over 47°C, PVA-C could potentially be used to create a phantom for RFA.

## 1.6 Polyvinyl alcohol

PVA has excellent properties for mimicking organs; it is non-toxic, has easily tailoring characteristics and strong mechanical resilience. It is a highly adaptable hydrophilic polymer without ionic properties, which means it ensures bio-compatibility, stability, and reproducibility, which makes it an ideal material for phantom construction. It simulates biological tissues and it is possible to perform medical and scientific experiments with it.[32]

To turn the PVA solution into a gel, the solution must be frozen and thawed repetitively. This is called a Freeze-Thaw (F-T) cycle and leads to PVA crystallization. The F-T process can be seen in Figure 2.[32]

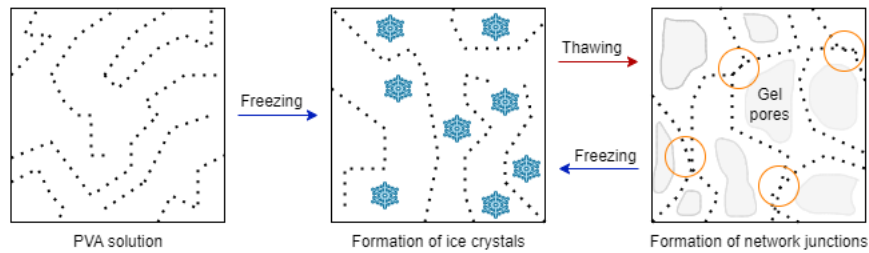


Figure 2: Schematic visualisation of the F-T process of a PVA solution. Starting with a solution containing PVA chains. Freezing this solution leads to the formation of ice crystals in between the PVA chains due to phase separation. Network junctions (circled in orange) will be formed during the thawing step. This establishes a gel network as the ice crystals become the pores of hydrogels.[32]

The properties of PVA can be influenced in multiple ways. As hydrogen bonds form between water and the hydroxyl groups of the PVA molecules, the PVA-C solidifies. A higher number of F-T cycles improves the mechanical strength, elasticity, water resistance, and gel stability, due to the increase of PVA crystallization.[32] However, this will decrease the conductivity of PVA, but will not have an effect on the permittivity.[7] Lower freezing temperatures and longer freezing times also lead to more strength and stiffness, due to the increase of the crystallinity. However, a longer duration might be necessary, because of the time-intensive procedure of the PVA crystallization. A higher concentration of PVA also leads to a stronger gel and thus improves the mechanical properties.[32] This will, however, lead to a decrease of permittivity and conductivity.[7] At last, a higher molecular weight of the PVA leads to mechanically tough gels. However, in the long term, PVA with a bit lower molecular weights will be more stable.[32] If necessary, all of these factors will be considered to adjust in order to create a mechanically strong phantom.

According to the research of Surry et al.[33], PVA-C serves as a tissue-mimicking material suitable for phantom construction. Their findings showed that a concentration of 10 wt% (weight percentage) PVA in water results in the most versatile phantom. Using this concentration, the phantom keeps its shape, has low viscosity and low shrinkage post-F-T cycles.[33] In addition to this, PVA-C is a temperature sensitive material, which makes it suitable for the validation of temperature distributions, especially in the range of 45 to 70°C. Over this range the  $T_1$  and  $T_2$  relaxation times appear to be linearly increasing with temperature. The PVA-C is not affected by lower temperatures and at higher temperatures it is thoroughly melted, which is why it is not affecting the relaxation times any further. Applying heat will cause the hydrogen bonds to break, resulting in a change of the PVA-C structure. The cryogel will become more liquid, which leads to higher  $T_1$  and  $T_2$  relaxation times. The PVA molecules have a melting point of approximately 200°C. Therefore, applying heat will not lead to disruptions in the PVA polymer. The most significant change in relaxation times due to increasing temperature has been observed in the 10 wt% samples subjected to 2 F-T cycles.[31]

## 1.7 Dielectric properties of the human heart

When applying an electromagnetic (EM) field to a material, the response is determined by the dielectric properties of a material; the electrical conductivity ( $\sigma$ ), and relative permittivity ( $\epsilon_r$ ).[5] The relative permittivity, or dielectric constant, can be defined as the ratio of stored electrical energy within a medium relative to a vacuum. The electrical conductivity can be seen as the ionic currents inside biological tissues and can be defined as the ability to transport charge.[7]

There is only few data available about these dielectric properties in the RF ablation frequency range. The electrical conductivity of muscle, which includes heart tissue, has been investigated at 500 kHz and between 40 and 90°C. It has been found that the conductivity increases with increasing temperature. Furthermore, when reaching a temperature higher than 60°C, irreversible alterations will occur in the tissue.[34]

To effectively perform RFA, it is essential to manipulate the dielectric properties of the heart. This study primary focuses on manipulating the conductivity, which can be achieved with certain potential additives. The research of Luik states that the addition of salt controls the conductivity of the phantom.[7] Besides salt, adding sodium acetate to the phantom resulted in an increase of conductivity. It has been found that diffusion of salt takes place when the phantom is stored in liquid. Storing the phantom in the same solution as it is prepared with, to mimic the conductivity of human blood, would solve this. A storage solution made of 0.15 wt% salt appeared to successfully mimic the conductivity of blood. Therefore, the phantom should be prepared with this same concentration. The dielectric properties of PVA-C could also be affected by water absorption, resulting in a decrease in permittivity and conductivity. Hence, it is important to take diffusion and absorption into account.

In addition to mimicking the conductivity, and even the permittivity, adding salt encourages interactions of polymer chains and disrupts the intra PVA chains. This leads to a shorter gelling time and a stiffer phantom, due to the increase in crystallinity.[7]

## 1.8 Aim

This study focuses on the development of a specialized dynamic heart phantom composed of PVA, with the addition of salt. This work shows if the phantom is suitable for the training and validation of RFA procedures, using  $T_1$  and  $T_2$  mapping techniques. The goal is to validate the procedure and improve RFA training and monitoring.

This leads to the following research question: *How does a specialized dynamic heart phantom, composed of PVA, perform in simulating the properties of the heart for training, and validating Radiofrequency Ablation (RFA) procedures, using  $T_1$  and  $T_2$  mapping techniques and how can it be further improved?*

## 2 Methods

### 2.1 Fabrication protocol

The phantom was made of, fully hydrolyzed, polyvinyl alcohol (Sigma Aldrich, ST. Louis, Missouri, USA), average MW 13.00-23.00 g/mol. The final mixture was composed of 10 wt% PVA, 0.15 wt% salt and tapwater. The addition of salt will ensure the manipulation of the dielectric properties of the heart. The solution was stirred by hand. After this, the solution was heated, while continuously stirring, to 90°C to make sure the powder was fully dissolved. The temperature must be kept below 100°C to reduce water loss.[35] After heating, the gel was cooled down, while stirring sometimes, to room temperature in order to complete the formation of the homogeneous gel.[33]

The mixture was poured into different molds, which went through two F-T cycles. The first step of the F-T cycle is freezing the solution. The solution was placed in a normal freezer and went from room temperature to approximately -20°C. It was kept at this temperature for 24 hours. After that, the phantom had a thawing time of 24 hours. This cycle was repeated twice to get the desired mechanical strength. The last step was to remove the phantom from the mold and put it in a storage solution of tapwater and 0.15 wt% salt, to prevent diffusion of salt out of the phantom.

### 2.2 3D ventricle mold design

To produce an artificial ventricle, a mold was designed in a 3D CAD program (Solidworks, Dassault Systèmes SolidWorks Corp., Massachusetts, United States), based on Ref [29]. Representing the left ventricle dimensions of healthy men; a 50 mm diameter at the basis, 10 mm wall thickness, 55 ml systolic volume and a ventricle length from base to apex of 75 mm.[29] This design was printed with polylactic acid (PLA) at the DesignLab (University of Twente, Enschede, The Netherlands). The design of the outer and inner mold can be seen in Figure 3 and 4.



Figure 3: Design of the outer mold for the left ventricle, representing normal dimensions for healthy men. This mold is needed in duplicate to create the entire outer cast for the left ventricle.



Figure 4: Design of the inner mold for the left ventricle, representing normal dimensions for healthy men.

### 2.3 Temperature calibration and MRI-based $T_1$ & $T_2$ relaxation

The relation between  $T_1$  and  $T_2$  relaxation times and temperature was characterized by using a set of spherical PVA phantoms. The phantom spheres consists of a mixture of 10 wt% PVA, 0.15 wt% salt and tapwater. The final mixture was poured into a tray containing 33 spherical molds, with a diameter of 2.8 cm each. After the phantom spheres went through 2 F-T cycles, the spheres were individually packed inside a plastic bag and placed in a temperature-controlled water bath to be heated to specific temperatures. A thermocouple was inserted in the center of each sphere to validate the temperature. The spheres were heated for 10 minutes each to ensure a consistent temperature. The procedure was repeated 21 times, with each time a different temperature setting. The temperature settings range from 43 to 62°C, with a reference temperature at 37°C.

After every sphere was heated to a different temperature, the tray with spheres was stored in the fridge in a plastic vacuum bag to prevent dehydration. 17 hours later the tray was scanned following the scanning protocol, which can be found in section 2.6. The acquired  $T_1$  and  $T_2$  times were combined with the temperature of the waterbath to model the alteration in  $T_1$  and  $T_2$  times with increasing temperature. The scans were repeated after two weeks to investigate the potential decay of temperature memory over time.

To perform the calibration in duplicate, 12 remaining phantom spheres were heated in a waterbath to different temperatures in the range of 44-62°C with a 2°C interval. One phantom sphere was heated to a temperature of 37°C for the lower bound of the curve and one to 70°C for the upper bound. The spheres were heated for 10 minutes each to reach a consistent temperature.

To investigate the effect of the addition of salt and the thawing rate, 30 microtubes were filled with only a 10 wt% PVA solution. Those microtube samples went through 2 F-T cycles of 24 hours each step. Half of the microtubes thawed immediately to room temperature, while the other half thawed in the refrigerator for the first five hours, to investigate the influence of the thawing rate. These microtube samples were heated in a waterbath to different temperatures in the range of 44-70°C with a 2°C interval and with a reference temperature at 37°C to get the full calibration curve. The microtubes were heated for 10 minutes each to reach a consistent temperature.

### 2.4 Needle ablation of a rectangular phantom

To validate temperature changes in 3D, the PVA and salt mixture was poured into a small box with a volume of approximately 200 mL. The F-T cycle was repeated two times, with a freezing time of 24 hours and a thawing time of 24 hours. The phantom cube was ablated with a needle four times at different, locations. The small electrode was inserted directly into the target material. Through the electrode, the RF energy was delivered, which heated the material and caused localized thermal damage. The ablation was performed at a power of 5W for multiple seconds leading to four specific temperatures; 50,5°C, 51°C, 55°C and 60°C. After ablation the ablated area was evaluated by obtaining 3D  $T_1$  and  $T_2$  maps. These maps were converted into temperature maps, using the calibration curves.

## 2.5 Radiofrequency catheter ablation of the heart phantom

The final heart phantoms were created by pouring the PVA and salt mixture into the ventricle molds and following the fabrication protocol. After this, they were stored in a solution made of tap water and 0.15 wt% salt to prevent diffusion.

The real RF catheter ablation was performed on one heart phantom. The phantom was ablated by a clinician. Five different settings were used to create five different lesions. The settings can be seen in Table 1.

Table 1: Different settings of the radiofrequency catheter ablations on the heart phantom

	First ablation	Second ablation	Third ablation	Fourth ablation	Fifth ablation
<b>Power (W)</b>	50	50	50	50	50
<b>Temperature (°C)</b>	60	55	50	60	55
<b>Time (s)</b>	30	30	30	10	10

The phantom was imaged following the scanning protocol, after which the generated 3D  $T_1$  and  $T_2$  maps were converted into temperature maps.

## 2.6 Scanning protocol

### 2.6.1 $T_1$ and $T_2$ mapping

$T_1$  and  $T_2$  mapping are MRI techniques used to quantitatively assess tissue properties based on the  $T_1$  and  $T_2$  relaxation times. The mapping of the different phantoms was performed on a Siemens 1.5T scanner (Aera, Siemens Healthineers, Erlangen, Germany). Table 2 shows the different settings of the two used sequences to create the  $T_1$  maps; 2D Inversion Recovery (IR) and 3D Inversion Recovery.

Table 2: Settings for the different sequences to obtain  $T_1$  maps.

Sequence	2D IR	3D IR
<b>FoV (mm)</b>	256 x 256 x 32	288 x 288 x 48
<b>Voxel size (mm)</b>	2.0 x 2.0 x 10.0	1.5 x 1.5 x 1.5
<b>TR (ms)</b>	1500.0	1500.0
<b>TE (ms)</b>	2.07	80.0
<b>TI (ms)</b>	200, 500, 800, 1100 & 1400	200, 500, 800, 1100 & 1400
<b>Slice thickness (mm)</b>	10.0	1.50
<b>Slices per slab</b>	1	32

The 3D  $T_1$  data has been obtained with an IR sequence. The obtained results were fitted using MATLAB® (R2023b, Mathworks, Natick, MA, USA). A generated mask defined the regions of interest (ROIs) for the  $T_1$  mapping. The mask was expanded by applying erosion using a disk-shaped element for the phantom spheres and a rectangular-shaped element for the rectangular and heart phantoms. ROIs were selected within this mask and the  $T_1$  values were estimated using a nonlinear curve fitting algorithm. Each pixel represents a specific  $T_1$  relaxation time in the generated  $T_1$  maps. The  $T_1$  relaxation times were calculated using the inversion recovery equation. The acquired TI was plotted against the fitted data. The generated  $T_1$  maps were used to analyse the ablated phantoms.

Table 3 shows the different settings of the three used sequences to create the  $T_2$  maps; 2D Spin Echo (SE) and 3D Fast Spin Echo (FSE).

Table 3: Settings for the different sequences to obtain  $T_2$  maps.

Sequence	2D SE	3D FSE
FoV (mm)	256 x 256 x 48	288 x 288 x 48
Voxel size (mm)	2.0 x 2.0 x 10.0	1.5 x 1.5 x 1.5
TR (ms)	1500.0	1000
TE (ms)	25.0 - 500.0 (in steps of 25 ms)	80, 160, 240, 320 and 400
Slice thickness (mm)	10.0	1.50
Slices per slab	1	48

The 3DFSE sequence was used to acquire the 3D MRI data. The data was processed using MATLAB® (R2023b, Mathworks, Natick, MA, USA). A mask for ROIs was created with the use of the minimum Cross-Entropy thresholding method and it was expanded by applying erosion. For the phantom spheres this erosion was using a disk-shaped element and for the rectangular and heart phantoms it was a rectangular-shaped element. Within this mask the ROIs were selected. For each pixel within the ROIs the  $T_2$  values were estimated using a nonlinear curve fitting algorithm. Each pixel represents a specific  $T_2$  relaxation time in the generated  $T_2$  maps. The generated  $T_2$  maps were used to analyse the ablated phantoms.

## 2.6.2 Temperature mapping

The 3D  $T_1$  and  $T_2$  maps were converted into temperature maps using the calibration curves. A linear model has been used to fit the  $T_1$  and  $T_2$  relaxation time data, which resulted in a linear equation:  $Y = aX + b$ . In this equation  $Y$  is the  $T_1$  or  $T_2$  value,  $X$  is the temperature,  $a$  is the slope and  $b$  is the intercept of the linear fit. Below a specified threshold the  $T_1$  values are converted to a default temperature for consistent temperature mapping, based on the reached equilibrium.[31] The linear fit has been applied to the specific slice of the 3D  $T_1$  and  $T_2$  maps to calculate the 2D temperature map.

## 3 Results

### 3.1 Temperature calibration with MRI-based $T_1$ and $T_2$ relaxation

The  $T_1$  map of the phantom spheres is presented in Figure 5. The temperature of the phantom spheres increases from the top sphere of the first column to the bottom sphere, to the top sphere of the second column, et cetera. The  $T_1$  relaxation time increases with increasing temperature, from approximately 1100 to 1350 ms. Figure 6 shows the  $T_2$  map of the phantom spheres. The  $T_2$  relaxation time slightly increases with increasing temperature from approximately 230 to 280 ms, after which it decreases to approximately 260 ms.

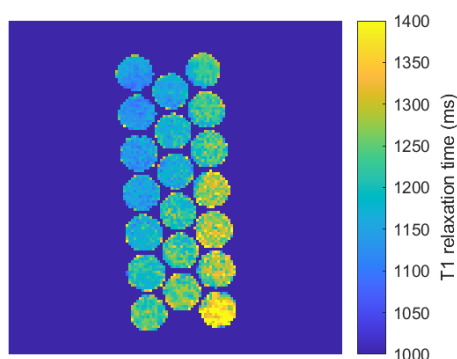


Figure 5: IR  $T_1$  map of the phantom spheres. An increase in  $T_1$  relaxation time can be observed, from approximately 1100 to 1350 ms, with increasing temperature (top left to bottom right column).

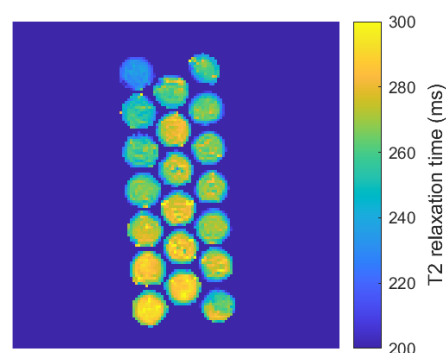


Figure 6: SE  $T_2$  map of the phantom spheres. A slight increase in  $T_2$  relaxation time can be observed from 230 to 280 ms with increasing temperature. At the last few spheres, the  $T_2$  relaxation time decreases to 260 ms.

The obtained data has been used to create the calibration curves, which can be seen in Figure 7 and 8. The relation between  $T_1$  and  $T_2$  relaxation times and temperature is assumed to be linear, which is why a linear fit has been used to calibrate the data.[31] The linear fit of the  $T_1$  relaxation time also includes an equilibrium point at temperatures below  $45^\circ\text{C}$ , because PVA is only temperature sensitive in the range of  $45^\circ\text{C}$  and  $70^\circ\text{C}$ .[31] The calibration curve of the  $T_2$  relaxation time lacks clear pattern, and deviates from a linear model. There is also no equilibrium point at the start of the curve. The scans have been repeated after two weeks to investigate a potential decay in temperature memory over time. In these graphs the standard deviation has been taken into account.

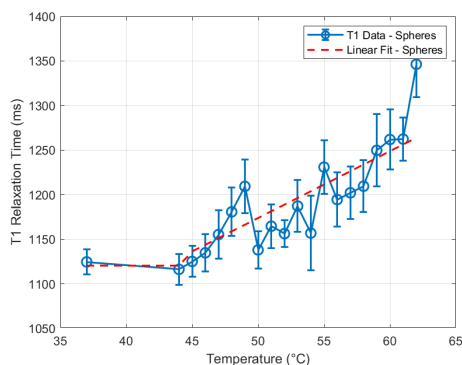


Figure 7: Calibration curve of the obtained  $T_1$  relaxation times. This graph shows the change in  $T_1$  relaxation time for the shown temperature range. The red dashed line shows the linear fit of the measurements including the equilibrium point at temperatures below  $45^\circ\text{C}$ .

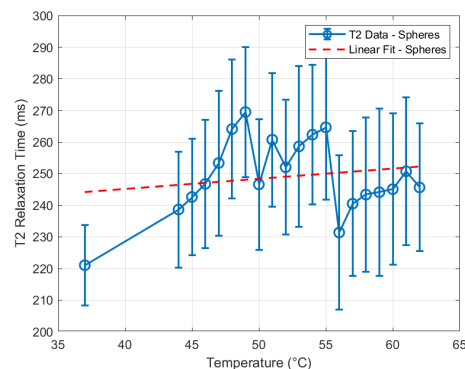


Figure 8: Calibration curve of the obtained  $T_2$  relaxation times. This graph shows the change in  $T_2$  relaxation time for the shown temperature range. The red dashed line shows the linear fit of the measurements.

The calibration experiment was repeated with 13 phantom spheres that went through 3 F-T cycles. Figure 9 shows the calibration curve of the  $T_1$  relaxation times of the repeated experiment. The  $T_1$  relaxation time increases from 1050 to 1300 ms. Figure 10 shows the calibration curve of the  $T_2$  relaxation times. The  $T_2$  relaxation time increases at first, after which it decreases and increases again. The starting  $T_2$  relaxation time is 180 ms and it increases to approximately 235 ms. The standard deviation has not been taken into account, because this measurement has only been performed and scanned once.

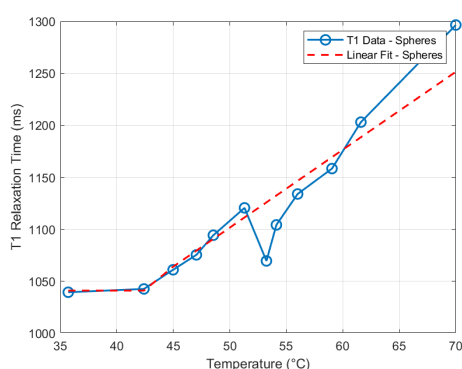


Figure 9: Calibration curve of the  $T_1$  relaxation times of the 3 F-T cycle phantom spheres. The graph shows an increase in  $T_1$  relaxation time in the temperature range of  $44$  to  $62^\circ\text{C}$ , with a starting point at  $37^\circ\text{C}$  and an end point at  $70^\circ\text{C}$ . The red dashed line shows the linear fit of the measurements including the equilibrium point at temperatures below  $45^\circ\text{C}$ .

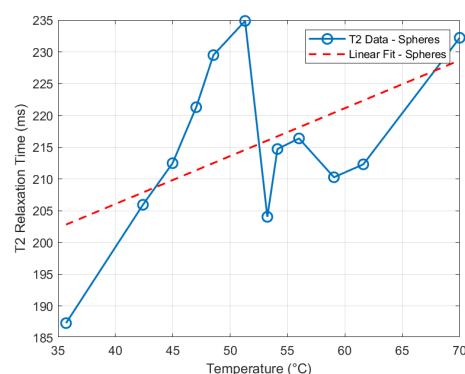


Figure 10: Calibration curve of the  $T_2$  relaxation times of the 3 F-T cycle phantom spheres. The graph shows the change in  $T_2$  relaxation time in the temperature range of  $44$  to  $62^\circ\text{C}$ , with a starting point at  $37^\circ\text{C}$  and an ending point at  $70^\circ\text{C}$ . The red dashed line shows the linear fit of the measurements.

The calibration experiment was also repeated with another mixture, without the addition of salt. Half of the microtubes was thawed more slowly, while the other half was thawed directly to room temperature. Figure 11 shows the two calibration curves of the  $T_1$  relaxation times. A linear increase in  $T_1$  relaxation time can be seen in both of the calibration curves. The slowly thawed microtubes show an increase from approximately 1250 ms to 1500 ms, while the fast thawed microtubes show an increase from approximately 1300 to 1500 ms. Figure 12 shows the two calibration curves of the  $T_2$  relaxation times. The changes in  $T_2$  relaxation times are random.

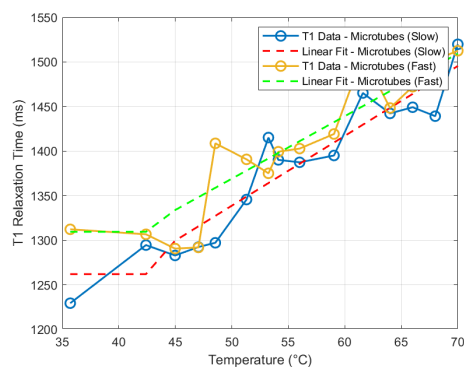


Figure 11: Calibration curves of the  $T_1$  relaxation times of the PVA microtubes. The graph shows an increase in  $T_1$  relaxation time in the temperature range of 44 to 70°C, with a starting point at 37°C. The dashed lines show the linear fits of the measurements including the equilibrium points at temperatures below 45°C.

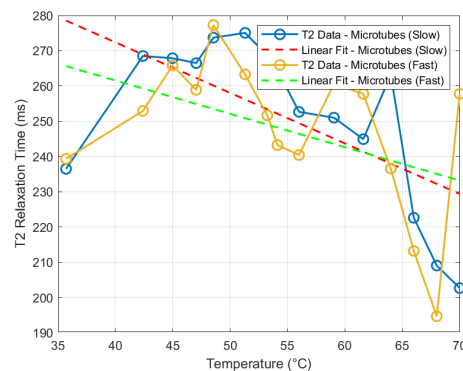


Figure 12: Calibration curves of the  $T_2$  relaxation times of the PVA microtubes. The graph shows the change in  $T_2$  relaxation time in the temperature range of 44 to 70°C, with a starting point at 37°C. The dashed lines show the linear fit of the measurements.

## 3.2 Needle ablation of a rectangular phantom

### 3.2.1 $T_1$ and $T_2$ 3D maps after needle ablation

Figure 13 shows the  $T_1$  map after the needle ablation, before applying erosion. Although it was not necessary, erosion has been applied to remove the heightened signal at the edges. The air-plastic-PVA transition could cause artefacts. This effect is minimized by applying erosion.[36] On all other  $T_1$  and  $T_2$  maps erosion has been applied. Figure 14 shows the top view of the  $T_1$  map. An increase in  $T_1$  relaxation time can be observed from approximately 1300 to a maximum of 1600 ms. The corresponding, real, ablated temperatures, in the figures of the top and front view, are, from top to bottom, 60°C, 55°C and 50.5°C and 51°C. The displayed slices do not display all of the ablated areas at their peak temperature.

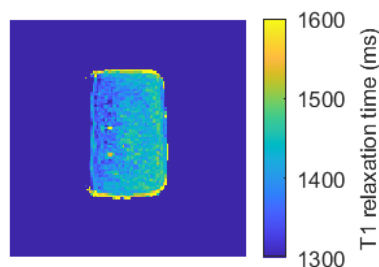


Figure 13: Top view of the  $T_1$  map after needle ablation, before applying erosion.

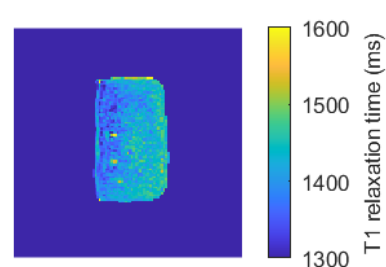


Figure 14: Top view of the  $T_1$  map after needle ablation. Displayed is slice 21. All four ablated areas are slightly visible. The  $T_1$  relaxation time increases from approximately 1300 to 1600 ms.

The front view of the  $T_1$  map can be seen in Figure 15. Three ablated areas are slightly visible with a  $T_1$  relaxation time of approximately 1518.5, 1640.9 and 1609.1 ms, from top to bottom. Figure 16 shows the side

view of the  $T_1$  map after needle ablation. One ablated spot is visible at the top, with a  $T_1$  relaxation time of 1640.9 ms.

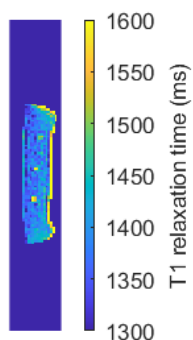


Figure 15: Front view of the  $T_1$  map after needle ablation. Displayed is slice 15. Three of the ablated areas are visible with increased  $T_1$  relaxation times.

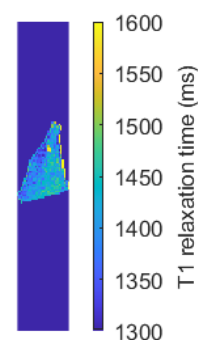


Figure 16: Side view of the  $T_1$  map after needle ablation. Displayed is slice 16. One ablated area is visible at the top, with an increased  $T_1$  relaxation time.

Figure 17 shows the top view of the  $T_2$  map of the rectangular phantom after needle ablation. The  $T_2$  relaxation time increases from approximately 200 to 400 ms with increasing temperature. The four ablated areas are visible within the displayed slice, with a  $T_2$  relaxation time of 320, 410, 330 and 305 ms, from top to bottom. Figure 18 shows the front view of the  $T_2$  map. All of the four ablated areas are visible with a relaxation time of 360, 410, 380 and 350 ms, from top to bottom.

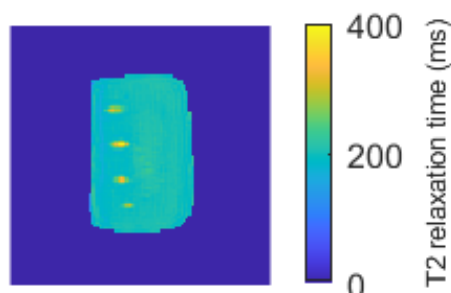


Figure 17: Top view of the  $T_2$  map after needle ablation. Displayed is slice 29. All of the four ablated areas are visible. The  $T_2$  relaxation time increases from approximately 200 to 400 ms.

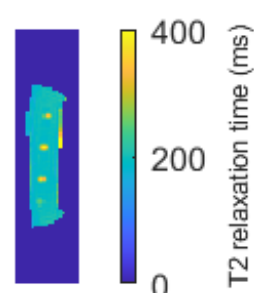


Figure 18: Front view of the  $T_2$  map after needle ablation. Displayed is slice 22. All of the four ablated areas are visible with increased  $T_2$  relaxation times.

Figure 19 shows the side view of the  $T_2$  map after needle ablation. One of the four ablated areas is clearly visible with a  $T_2$  relaxation time of 410 ms.

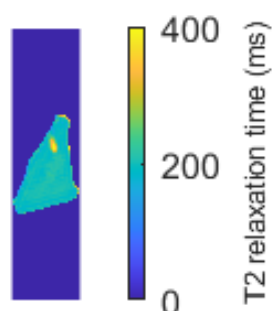


Figure 19: Side view of the  $T_2$  map after the needle ablation. Displayed is the central slice, slice 24. An ablated spot with a  $T_2$  relaxation time of 410 ms can be seen in the top of the phantom.

### 3.2.2 Temperature maps after needle ablation

The temperature maps have been generated by converting the 3D  $T_1$  and  $T_2$  using the calibration curves. Figure 20 shows the temperature map based on the obtained  $T_1$  calibration curve. Three ablated areas are slightly visible with a minimum temperature of 62.2°C and a maximum temperature of 69.1°C. Figure 21 shows the temperature map based on the obtained  $T_2$  calibration curve. All of the ablated areas reach a minimum temperature of 60 °C, with a maximum of 70°C.

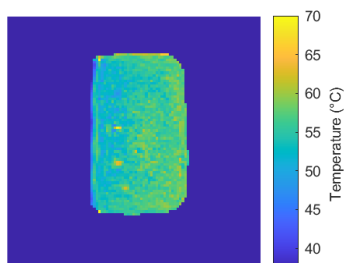


Figure 20: Temperature map based on the  $T_1$  linear fit. Displayed is slice 21. The temperature increases to 69.1°C in the most visible ablated spot.

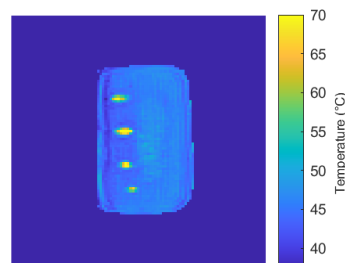


Figure 21: Temperature map based on the  $T_2$  linear fit. Displayed is slice 29. All of the ablated spots reach a temperature of 70°C.

### 3.3 Catheter ablation of the heart phantom

#### 3.3.1 3D $T_1$ and $T_2$ maps after RFA

The front and top view of the 3D  $T_1$  map can be seen in Figure 22 and 23. One ablated spot is clearly visible. The  $T_1$  relaxation time increases from approximately 1200 ms to a maximum of 2639.61 ms.

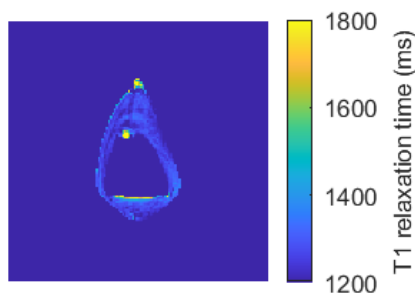


Figure 22: Front view of the  $T_1$  map after RFA. Displayed is slice 35.

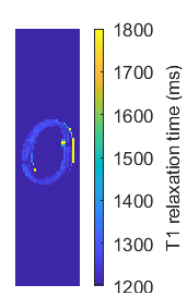


Figure 23: Top view of the  $T_1$  map after RFA.

The front and top view of the 3D  $T_2$  map can be seen in Figure 24 and 25. In the front view, the ablated spot is clearly visible and the  $T_2$  relaxation time increases from approximately 190 ms to 1000 ms. The top view only slightly shows the ablated spot at which a  $T_2$  relaxation time of 250 ms has been reached.

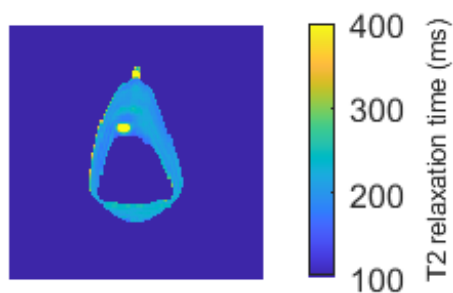


Figure 24: Front view of the  $T_2$  map after RFA. Displayed is slice 35. One ablated spot is visible with a  $T_2$  relaxation time of 1000 ms.

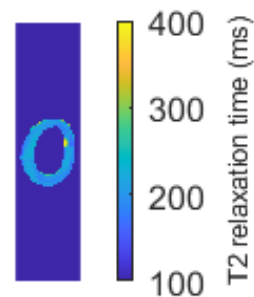


Figure 25: Top view of the  $T_2$  map after RFA. The ablated spot has a  $T_2$  relaxation time of 250 ms.

### 3.3.2 Temperature maps after RFA

The temperature maps of the heart phantom have been generated by converting the 3D  $T_1$  and  $T_2$  maps, using the calibrated linear fits. Figure 26 and 27 show the front and top view of the temperature maps based on the  $T_1$  linear fit. According to the linear fitted model, the ablated region surpasses  $70^\circ\text{C}$  in temperature.

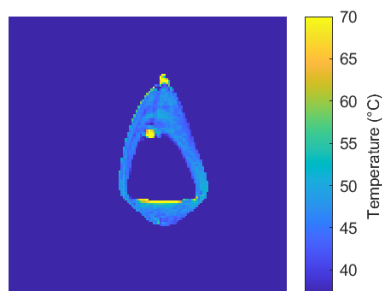


Figure 26: Front view of the temperature map based on the  $T_1$  calibration curve. Displayed is slice 35.

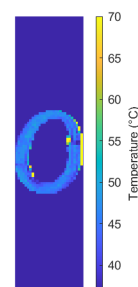


Figure 27: Top view of the temperature map based on the  $T_1$  calibration curve.

A 3D rendering of these  $T_1$  temperature maps of the ablation is presented in Figure 28. This map shows the localized ablation lesion.

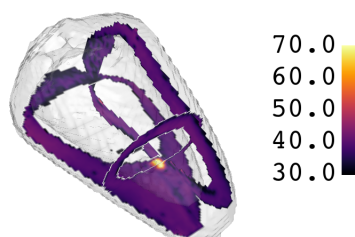


Figure 28: 3D rendering of the  $T_1$  temperature map. The lesion is clearly visible with a temperature of  $>70^\circ\text{C}$ , according to the linear fitted model.

The front and top view of the temperature maps based on the  $T_2$  calibration curve can be seen in Figure 29 and 30. As per linear fitted model, the ablated area exceeds a temperature of  $>70^\circ\text{C}$ .

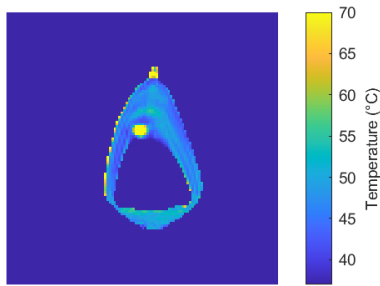


Figure 29: Front view of the temperature map based on the  $T_2$  calibration curve. Displayed is slice 35.

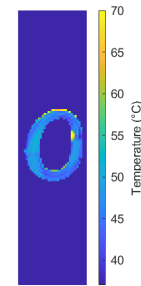


Figure 30: Top view of the temperature map based on the  $T_2$  calibration curve.

## 4 Discussion

### 4.1 Fabrication protocol

#### 4.1.1 Number of F-T cycles

Two phantoms were created which went through a different number of F-T cycles. The first one went through 2 F-T cycles and the second phantom went through 3 F-T cycles. Both had a freezing and thawing time of 24 hours each cycle. The phantom that went through 3 F-T cycles seems to be mechanically stiffer. Further investigation is required to determine whether the increased mechanical stiffness is essential for a better simulation of the properties of the heart. This involves an assessment of the Young's Modulus, which should be in the range of 10 kPa - 50 kPa for a cardiac phantom.[7] According to Luik et al.[7] a 10% PVA phantom that went through 1 F-T cycle has a Young's Modulus of  $25 \pm 4$  kPa. This would already be in the correct range, and thus, three F-T cycles would be unnecessary.[7]

A higher number of F-T cycles also slightly influences the relaxation times. Increasing the number of F-T cycles results in lower  $T_1$  and  $T_2$  relaxation times. When the number of F-T cycles increases, more ice crystals will be formed.[32] This restricted water mobility results in a shorter  $T_1$  relaxation time. The presence of ice crystals alters the interactions between surrounding water molecules, resulting in a decrease in  $T_2$  relaxation time. An extra F-T cycle leads to a decrease in  $T_1$  relaxation time of approximately 100 ms and to a decrease in  $T_2$  relaxation time of approximately 30 ms. It is important to create the phantoms following the exact same fabrication protocol to prevent differences in starting  $T_1$  and  $T_2$  relaxation times.

#### 4.1.2 F-T cycle time

The F-T cycle time influences the mechanical strength of the phantom, as explained in Section 1.6. The first created reference phantom went through two F-T cycles with different freezing and thawing times. The freezing times were approximately 6 hours and the thawing times approximately 17 hours. This resulted in a mechanically weak phantom. This could be caused by the short freezing times, which were not long enough for the time-intensive crystallization procedure.[32] After two F-T cycles, the phantom was put in the freezer for 72 hours to continue the crystallization, resulting in a mechanically strong phantom. The next phantoms went through two F-T cycles of 24 hours freezing and 24 hours of thawing time each cycle, which resulted in mechanically strong phantoms.

#### 4.1.3 Different used PVA powder

Two phantoms have been created with different PVA powder to investigate the influence on the mechanical properties of the phantom. The first phantom (Sigma Aldrich, ST. Louis, Missouri, USA) is fully hydrolyzed and has an average molecular weight (MW) of 13.00-23.00 g/mol. The second phantom (Kuraray, Tokyo, Japan) is also fully hydrolyzed, but has an average MW of 31.00 g/mol. The first phantom had unreliable F-T cycles, while the second phantom went through two F-T cycles of 24 hours of each step. This makes the comparison a bit more difficult. However, after those different F-T cycles, there was no clear difference

between the mechanical strength of both phantoms. The choice was made to continue with the Sigma Aldrich PVA powder. A third phantom, created of this PVA powder, went through two F-T cycles of 24 hours of each step. The mechanical strength did not seem to differ from the previous ones, which should exclude the influence of using a different PVA powder. This assessment did not include testing the Young's modulus, which should be done when investigating the mechanical stiffness.

## 4.2 Heating of the phantoms

### 4.2.1 Temperature of the phantom spheres

The phantom spheres were heated in a water bath to different temperatures. It has appeared that the spheres would not reach the desired temperature within 10 minutes. A uniform temperature could have been achieved when heating the spheres for 12 minutes each.[30] However, when taking the accuracy of  $2^{\circ}\text{C}$  into account, the temperature could be slightly off. This could be as much as  $2^{\circ}\text{C}$  in either direction. This means that either the temperature does reach closer to the desired temperature or it is even further away from the desired temperature. Many of the reached temperatures varied more than  $2^{\circ}\text{C}$  with the desired temperatures, with an average of  $3.4^{\circ}\text{C}$ . The temperature indicated by the thermometer also did not match with the temperature of the waterbath. The thermometer turned out to have an empty battery. This variances would cause an inaccurate calibration curve, because the  $T_1$  and  $T_2$  maps show an increase in relaxation times, while the temperature does not change much. To create the calibration curve, the temperature of the waterbath has been used to prevent large inaccuracies. When repeating the calibration experiment, a fiber temperature sensor has been used. This fiber has an accuracy of  $\pm 0.3^{\circ}\text{C}$ . However, this calibration can not be used, because the ablation phantoms have been created differently. The calibration experiment should be repeated with the 2 F-T cycle phantom spheres, including the fiber temperature sensor.

### 4.2.2 Melting point

Every phantom sphere was supposed to be heated to a specific target temperature in the range of 44 to  $75^{\circ}\text{C}$ . However, when a temperature of  $62^{\circ}\text{C}$  was reached, the small sphere was starting to melt. The melting point of PVA molecules is about  $200^{\circ}\text{C}$ , which is greater than the reached temperature of  $62^{\circ}\text{C}$ . Lukas et al.[31] showed the presence of an equilibrium point above  $70^{\circ}\text{C}$ , caused by the entirely melted PVA. The melting would be due to the disruption of the hydrogen bonds created in the F-T cycles and not the PVA polymer itself.[31] These melting temperatures do not completely correspond, while both mixtures consist of 10 wt% PVA and went through 2 F-T cycles. A difference in composition is the addition of salt, which could reduce the crystallinity of PVA, resulting in insufficient internal bonding strength.[37] The disruption of the polymer chains will weaken the PVA-C structure. This alteration in the structure could enable a lower melting point for the material. However, adding salt is necessary to mimic the conductivity. The exclusion of salt only leads to a minor decrease in  $T_1$  and  $T_2$  relaxation times, but the melting point does not seem to be affected.

Increasing the number of F-T cycles enhances interactions between water and PVA molecules, leading to stronger bonding.[38] When the spheres reached the melting point, the remaining spheres were put into the freezer to go through another F-T cycle. Unfortunately, this did not result in a higher melting point. As a preventative measure, it is suggested to create samples in a tube to perform a complete calibration.

## 4.3 $T_1$ and $T_2$ relaxation times vs. temperature

### 4.3.1 Calibration of $T_1$ and $T_2$ relaxation times

The applied heat ensures the breaking of hydrogen bonds, which disrupts the cross-links created in the F-T cycles. This leads to a structural change of PVA-C, resulting in elevated  $T_1$  and  $T_2$  relaxation times, because the cryogel becomes more liquid.[31] The results of the phantom spheres show an increase in  $T_1$  relaxation time. A linear fit has been used to calibrate the data, because the research of Lukas et al.[31] showed a linear relationship between  $T_1$  relaxation time with increasing temperature.[31] The obtained  $T_2$  data only shows a slight increase and it even decreases again. The linear fit only shows a small, averaged increase. This calibration curve deviates from a linear model, as found in the literature.[31]

The generated temperature map of the rectangular phantom based on the  $T_1$  linear fitted model visualizes three ablated areas. A minimum temperature of  $62.2^\circ\text{C}$  and a maximum temperature of  $69.1^\circ\text{C}$  have been reached. While the real ablated temperatures reach between  $50^\circ\text{C}$  and  $60^\circ\text{C}$ . The ablated spot in the temperature map of the heart phantom, based on  $T_1$  mapping, reaches a temperature of  $>70^\circ\text{C}$ . There are some inaccuracies in the  $T_1$  fit. Figure 31 shows the signal intensity curve of a random pixel. The fitted model follows the real data accurately. Figure 32 shows the signal intensity curve inside the lesion and fits the pixel with the highest  $T_1$  relaxation time. This fitted model slightly deviates from the real data. The inaccurate fit could result in higher temperatures than the ablated temperatures. This might be solved by using more TI's, which would give a more accurate fit. The temperature maps converted from the 3D  $T_1$  mapping clearly visualizes the ablated areas, but the temperature validation is inaccurate.

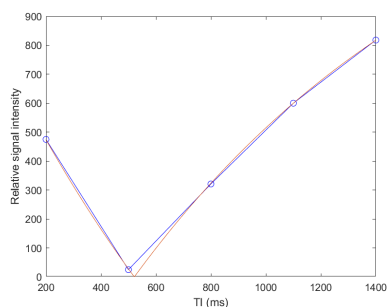


Figure 31: Signal intensity curve of a random pixel.

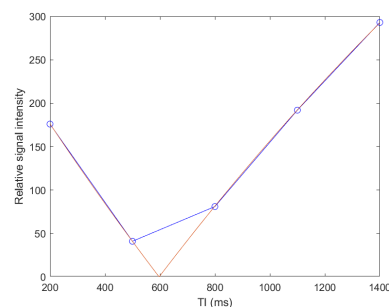


Figure 32: Signal intensity curve of the pixel with the highest  $T_1$  relaxation time.

The obtained data of the  $T_2$  relaxation times can not be used as a representative calibration curve of the  $T_2$  mapping. The 2 F-T cycle calibration curve shows an averaged linear fit, which would always result in temperature maps with higher temperatures than the real ablated temperature. The data in the 3 F-T cycle calibration curve also deviates from a linear model. The calibration curves of the phantoms without salt show random data points. This observation does not correspond with the research of Lukas et al.[31], which shows a clear linear model. The ablated areas in the temperature map of the rectangular phantom have reached a temperature of  $70^\circ\text{C}$ , while the maximum temperature actually is  $60^\circ\text{C}$ . The temperature map of the cardiac phantom based on the  $T_2$  linear fitted model also shows temperatures of  $>70^\circ\text{C}$ . This can be explained by the difference in heating rate. A gradual heating, like the calibration experiment, results in more subtle alterations in material structure, leading to a relative minor increase in  $T_2$  relaxation times. After needle ablation and RFA, the rapid and intense heating can lead to more notable changes in the structure and thus to a significant increase in  $T_2$  relaxation times.[18] Nevertheless, the  $T_2$  calibration curve can not be used during this study to validate the ablated temperatures.

Three other calibration experiments have been performed. One with spherical phantoms that went through 3 F-T cycles, and two with only a PVA mixture in microtubes. Half of these microtubes thawed directly to room temperature, while the other half thawed slower. The  $T_1$  and  $T_2$  relaxation time are affected by the addition of salt. Adding salt to the mixture will slightly lower the  $T_1$  and  $T_2$  relaxation times.[39] The starting  $T_1$  and  $T_2$  relaxation times when including salt are 1150 ms and 220 ms, respectively. While the starting  $T_1$  and  $T_2$  relaxation times without adding salt are approximately 1300 ms and 240 ms, respectively. All the  $T_1$  relaxation time calibration curves seem linear, starting at an equilibrium, just like the literature.[31] It is not clear if it also ends with an equilibrium after  $70^\circ\text{C}$ , because this lies outside the used temperature range. It is recommended to repeat the calibration experiment within a larger range of temperatures to create a complete calibration curve.

The thawing rate slightly affects the calibration curves. A slower thawing rate leads to a slightly lower  $T_1$  calibration curve. The effect on the  $T_2$  relaxation time is unclear. The differences are not significant. It is possible, but not necessary, to exclude salt from the mixture or change the thawing rate, as long as all the phantoms are made following the same fabrication protocol. Further research should include a thermocouple for temperature logging during the F-T cycles, providing more precise data about the thawing and freezing rates.

### 4.3.2 Variance in $T_1$ and $T_2$ relaxation times

The 2D  $T_1$  map of the phantom spheres shows an increase in  $T_1$  relaxation time from approximately 1100 to 1300 ms. The 3D  $T_1$  maps of the rectangular phantom also show a slight increase from approximately 1300 to 1600 ms, while the 3D  $T_1$  maps of the cardiac phantom show a significant increase from 1250 to 2600 ms. The 2D  $T_2$  map of the phantom spheres only shows a slight increase in  $T_2$  relaxation time. However, the 3D maps of the rectangular phantom show an almost twofold increase in the  $T_2$  relaxation time within the ablated areas. Also the 3D  $T_2$  map of the cardiac phantom shows a significant increase in  $T_2$  relaxation time. The ablated areas can definitely be visualised by 3D  $T_1$  and  $T_2$  mapping. However, after converting these 3D maps into temperature maps, the temperature validation is inaccurate. This study primary focused on the  $T_1$  mapping.

One of the problems to take into account when using PVA-C to create a phantom is the long-term stability.[40] The  $T_1$  and  $T_2$  relaxation times may change over time. The potential decay of temperature memory over time has been investigated by repeating the scans of the phantom spheres after two weeks. The measurements show a decrease in  $T_1$  and  $T_2$  relaxation times with an average of 32.3 and 30.7 ms, respectively. The average of the standard deviations of the  $T_1$  was 27.0 ms and of the  $T_2$  21.7 ms. The differences are not significant, but it indicates different variability's of the  $T_1$  and  $T_2$ . The long-term stability of unheated phantoms have not been investigated. This could affect the accuracy and reliability of the experiments, causing differences in  $T_1$  relaxation times between the different phantoms. However, the  $T_1$  relaxation time exhibits an increase instead of a decrease after several weeks. The long-term stability of the phantoms should be further investigated to clarify these differences.

The  $T_1$  relaxation time can also be influenced by the size of the material, affecting the distribution of PVA and salt.[41] The three created phantoms differ significantly in size. It is possible that larger phantoms have a different PVA and salt distribution, which may lead to variations in the microstructure and, thus, in  $T_1$  relaxation times. The unablated rectangular phantom corresponds with a  $T_1$  relaxation time of 1350 ms, the unablated cardiac phantom has a  $T_1$  relaxation time of 1250 ms and the phantom sphere at 37°C has a  $T_1$  relaxation time of 1134 ms. This could indicate a better distribution inside a smaller phantom, leading to a lower  $T_1$  relaxation time. To prove this hypothesis, the phantoms should be scanned pre-heating.

Another difference during the experiments was the storage of the phantoms. The phantom spheres were stored in a plastic tray inside a vacuum bag, the rectangular phantom was stored in a plastic box and the cardiac phantom was stored in a storage solution of tapwater and salt. Storing the phantom in a storage solution prevents dehydration of the phantom and avoids air contact.[7] Dehydration of the phantom typically results in a decrease of  $T_1$  relaxation time.[42] This would not explain the heightened starting  $T_1$  relaxation time of the rectangular phantom. This factor requires additional investigation by consistent storing conditions for the phantoms.

There are multiple possible explanations for the variance in  $T_1$  relaxation times of the different experiments. It is recommended to repeat all the experiments with phantoms following the exact same fabrication protocol, to scan the phantoms pre-heating, to perform experiments at the same period of time, and to store the phantoms in the same storage solution.

### 4.3.3 Re-usability of the phantom

A phantom used for RFA can only be used once, because of its temperature memory. The temperature is embedded in the phantom, which ensures the temperature validation. Unfortunately, this is also the reason an RFA phantom is not re-usable. A potential method for the re-usability of the phantom has been investigated. The ablated rectangular phantom went through another F-T cycle to investigate if the PVA will restructure, leading to a recovery of the  $T_1$  and  $T_2$  relaxation times. This was not the case, which means that the phantom will not be re-usable again.

## 4.4 Measurement errors and artefacts

### 4.4.1 Systematic error needle ablation

The accuracy of the device used to perform the needle ablation remained uncertain, introducing the possibility of consistently higher or lower temperature readings. This leads to a systematic error in the data compromising the reliability and trustworthiness of the results, due to the lack of accuracy and potential systematic error. This error should be taken into account when analysing the data.

### 4.4.2 Material transitions

The spherical phantoms are imaged inside a plastic tray and the cube phantoms inside a plastic box. This air-plastic-PVA transition can lead to a change in material properties and thus to measurement errors or artefacts.[36]. This artefact can be removed by applying erosion. If erosion has been applied the edges are not taken into account. The edge of the phantom in Figure 13 gives a higher signal than it is supposed to, due to the air-plastic-PVA transition. This artefact is not affecting the results, so applying erosion was not necessary. However, erosion has been applied on the  $T_1$  and  $T_2$  maps of the needle ablation. Although it does not affect the results, the higher signal at the edges was not desirable.

## 4.5 Further research recommendations

### 4.5.1 Dissolvable inner mold

To improve the 3D design of the ventricle mold, the inner mold could be printed with solid, thermoplastic PVA Filament using an Ultimaker 3 FDM printer. This has certain advantages in comparison to the normal printed inner mold. PVA Filament is water-soluble, which causes the inner mold to dissolve in water at a temperature of approximately 37°C. The PVA should be dissolved after about three hours. This easy removal ensures the mechanical strength and architecture of the phantom to be maintained.[43][44] The PLA inner mold must break in order to be removed from the phantom, which causes small cracks in the phantom. A PVA mold is also stable and resilient in hydrogels.[45] A potential disadvantage of using PVA filament to print the inner mold is the temperature memory of PVA-C. The temperature at which the inner mold dissolves will be embedded in the phantom. Although this temperature should not exceed 37°C, it is to be seen if temperature validation is still possible after using the phantom for ablation therapies. Furthermore, water absorption and diffusion should be taken into account. The PVA should be dissolved in a water bath, containing 0.15 wt% salt, otherwise the electromagnetic properties of the phantom could be altered.

### 4.5.2 Real-time MRI guidance and MR thermometry

The performed RFA on the final cardiac phantom was not image guided, leading to random placements of the catheter. The ablated spots could not be linked to the correct settings and temperatures. It is recommended to repeat this experiment guided by MRI to improve precision and have real-time feedback during the procedure. It is also important to take the dynamic aspect of the phantom into account, which may decrease the image quality caused by motion artefacts.[46]

The temperature validation with  $T_1$  weighted imaging has certain limitations.  $T_1$  weighted imaging is primarily focused on tissue contrast based on  $T_1$  relaxation time, not the measurement of absolute temperature values. These images offer qualitative indications of temperature distributions. However, they may lack the precision and sensitivity needed for accurate measurement of minimal temperature variations.[18] Other MRI techniques, like the PRF shift, should be used for precise temperature mapping. It is also recommended to repeat the RFA experiment with an inserted temperature sensor fiber in the phantom to investigate the real reached temperature.

The ultimate goal is to validate the temperature changes within the phantom by using MR thermometry. MR thermometry provides non-invasive, real-time temperature monitoring during RFA.[20] To ensure its reliability and accuracy, this method needs to be validated. An important part of this validation is the calibration of the MRI signal and corresponding temperatures. This calibration includes acquiring MRI images at varying, known temperatures. To track temperature changes in the phantom, MRI images are acquired before, during and after

RFA. These temperature changes are validated by inserting a temperature sensor inside the phantom to check if the MR thermometry matches the real temperatures in the phantom. This data is examined to investigate the accuracy of MR thermometry and if it is close enough to the real temperatures. To ensure a consistent method, the tests need to be performed multiple times.[47]

There are certain challenges in validating MR thermometry. At first, all of the properties of the PVA phantom must closely mimic those of the heart, because different tissue types have different characteristics which can impact MR thermometry measurements. These properties were taken into account, but not determined during this study. However, the PRF method is independent of tissue type, which makes it advantageous to use this method.[20] Secondly, the dynamic aspect of the phantom must be taken into account. The dynamic movements of the heart may change the position, shape and orientation of the target tissue and could affect the accuracy of MR thermometry. The error, caused by cardiac motion, could have a standard deviation of more than  $\pm 10$  °C, even without heat being applied. A potential solution is the employment of multi-baseline methods. This involves the acquirement of multiple reference images during the cardiac cycle. This strategy ensures precise alignment of the measured phase during the procedure with the appropriate reference image. Finally, the devices used for RFA can disrupt the magnetic field. This may lead to susceptibility artifacts. It is crucial to investigate different devices for potential MRI artifacts that could affect the accuracy of MR thermometry results to ensure the generalizability of the findings and reliable temperature monitoring.[48] The use of MR thermometry during the RFA procedure must be further investigated, taking all the challenges into account.

## 5 Conclusion

In this study, a dynamic heart phantom has been developed that simulates the properties of the heart. This phantom can potentially be used for training and validating RFA procedures, as the  $T_1$  relaxation time linearly increases with temperature. Temperature maps derived from  $T_1$  mapping enable the visualization of the ablated regions. Although, the precise temperature of the ablated areas can not yet be validated correctly. The outcomes of this research can be used as a basis for the development of monitoring techniques and as a resource for training programs.

## References

- [1] Lippi G, Sanchis-Gomar F, Cervellin G. Global epidemiology of atrial fibrillation: An increasing epidemic and public health challenge. *International Journal of Stroke*. 2020 Jan;16(2):217-21. doi:10.1177/1747493019897870.
- [2] Desai DS, Hajouli S. Arrhythmias. In: StatPearls [Internet]. StatPearls Publishing; 2023. Available from: <https://www.ncbi.nlm.nih.gov/books/NBK558923>.
- [3] What Is an Arrhythmia?; 2022. [Online; accessed 29. Aug. 2023]. Available from: <https://www.nhlbi.nih.gov/health/arrhythmias>.
- [4] Fu Dg. Cardiac Arrhythmias: Diagnosis, Symptoms, and Treatments. *Cell Biochem Biophys*. 2015 Nov;73(2):291-6. doi:10.1007/s12013-015-0626-4.
- [5] Salahuddin S, La Gioia A, Shahzad A, Elahi MA, Kumar A, Kilroy D, et al. Demonstration of dielectric heterogeneity of previously assumed homogeneous tissues: Examination of the heart. In: 12th European Conference on Antennas and Propagation (EuCAP 2018). IET; 2018. p. 1-5. doi:10.1049/cp.2018.0766.
- [6] Toupin S. Cardiac MR thermometry for the monitoring of radiofrequency ablation;.
- [7] Luik P. Design of a cardiac phantom for development of electrophysiology studies [Master's thesis]. Delft; 2023.
- [8] Dorn L, Kranzburg A, Saumell A, Gregory T, Reich S. Radiofrequency catheter ablation for atrial fibrillation. *JAAPA*. 2015 May;28(5):40. doi:10.1097/01.JAA.0000464275.36493.2d.
- [9] Grubb NR, Furniss S. Science, medicine, and the future: Radiofrequency ablation for atrial fibrillation. *BMJ*. 2001 Mar;322(7289):777. doi:10.1136/bmj.322.7289.777.
- [10] Kolandaivelu A, Zviman MM, Castro V, Lardo AC, Berger RD, Halperin HR. Noninvasive Assessment of Tissue Heating During Cardiac Radiofrequency Ablation Using MRI Thermography. *Circulation: Arrhythmia and Electrophysiology*. 2010 Oct. Available from: <https://www.ahajournals.org/doi/10.1161/CIRCEP.110.942433>.
- [11] Tungjitkusolmun S, Woo EJ, Cao H, Tsai JZ, Vorperian VR, Webster JG. Thermal—electrical finite element modelling for radio frequency cardiac ablation: Effects of changes in myocardial properties. *Med Biol Eng Comput*. 2000 Sep;38(5):562-8. doi:10.1007/BF02345754.
- [12] Kotadia ID, Williams SE, O'Neill M. High-power, Short-duration Radiofrequency Ablation for the Treatment of AF. *Arrhythmia Electrophysiol Rev*. 2020 Feb;8(4):265-72. doi:10.15420/aer.2019.09.
- [13] Zaltieri M, Massaroni C, Cauti FM, Schena E. Techniques for Temperature Monitoring of Myocardial Tissue Undergoing Radiofrequency Ablation Treatments: An Overview. *Sensors (Basel)*. 2021 Feb;21(4):1453. doi:10.3390/s21041453.
- [14] Mertyna P, Dewhirst MW, Halpern E, Goldberg W, Nahum Goldberg S. Radiofrequency ablation: The effect of distance and baseline temperature on thermal dose required for coagulation. *Int J Hyperthermia*. 2008 Jan;24(7):550-9. doi:10.1080/02656730802035662.
- [15] Calkins H, Hindricks G, Cappato R, Kim YH, Saad EB, Aguinaga L, et al. 2017 HRS/EHRA/E-CAS/APHRS/SOLAECE expert consensus statement on catheter and surgical ablation of atrial fibrillation. *Heart Rhythm*. 2017 Oct;14(10):e275-444. doi:10.1016/j.hrthm.2017.05.012.
- [16] Katti G, Ara SA, Shireen A. Magnetic Resonance Imaging (MRI) - A Review. *International journal of dental clinics*. 2011.
- [17] Chung AH, Jolesz FA, Hynynen K. Thermal dosimetry of a focused ultrasound beam in vivo by magnetic resonance imaging. *Med Phys*. 1999 Sep;26(9):2017-26. doi:10.1118/1.598707.

- [18] Nelson TR, Tung SM. Temperature dependence of proton relaxation times in vitro. *Magn Reson Imaging*. 1987 Jan;5(3):189-99. doi:10.1016/0730-725X(87)90020-8.
- [19] Kim PK, Hong YJ, Im DJ, Suh YJ, Park CH, Kim JY, et al. Myocardial T1 and T2 Mapping: Techniques and Clinical Applications. *Korean J Radiol*. 2017 Jan;18(1):113. doi:10.3348/kjr.2017.18.1.113.
- [20] Rieke V, Pauly KB. MR Thermometry. *Journal of magnetic resonance imaging : JMRI*. 2008 Feb;27(2):376. doi:10.1002/jmri.21265.
- [21] Vigen KK, Jarrard J, Rieke V, Frisoli J, Daniel BL, Pauly KB. In vivo porcine liver radiofrequency ablation with simultaneous MR temperature imaging. *J Magn Reson Imaging*. 2006 Apr;23(4):578-84. doi:10.1002/jmri.20528.
- [22] Jonathan Dornell P. In Vivo vs In Vitro: Definition, Pros and Cons. *Drug Discovery from Technology Networks*. 2022 Mar. Available from: <https://www.technologynetworks.com/drug-discovery/articles/in-vivo-vs-in-vitro-definition-pros-and-cons-350415>.
- [23] Lee FT, Haemmerich D, Wright AS, Mahvi DM, Sampson LA, Webster JG. Multiple Probe Radiofrequency Ablation: Pilot Study in an Animal Model. *J Vasc Interv Radiol*. 2003 Nov;14(11):1437-42. doi:10.1097/01.RVI.0000096771.74047.C8.
- [24] Knight WE, Ali HR, Nakano SJ, Wilson CE, Walker LA, Woulfe KC. Ex vivo Methods for Measuring Cardiac Muscle Mechanical Properties. *Front Physiol*. 2020;11. doi:10.3389/fphys.2020.616996.
- [25] Robinson D. The Phantoms of Medical and Health Physics. *Med Phys*. 2016 Sep;43(9):5264. doi:10.1118/1.4960370.
- [26] DeWerd LA, Lawless M. Introduction to Phantoms of Medical and Health Physics; 2014. doi:10.1007/978-1-4614-8304-5\_1.
- [27] Antoniou A, Damianou C. MR relaxation properties of tissue-mimicking phantoms. *Ultrasonics*. 2022 Feb;119:106600. doi:10.1016/j.ultras.2021.106600.
- [28] Lamouche G, Kennedy BF, Kennedy KM, Bisailon CE, Curatolo A, Campbell G, et al. Review of tissue simulating phantoms with controllable optical, mechanical and structural properties for use in optical coherence tomography. *Biomed Opt Express*. 2012 Jun;3(6):1381. doi:10.1364/BOE.3.001381.
- [29] Dieringer MA, Hentschel J, de Quadros T, von Knobelsdorff-Brenkenhoff F, Hoffmann W, Niendorf T, et al. Design, construction, and evaluation of a dynamic MR compatible cardiac left ventricle model. *Med Phys*. 2012 Aug;39(8):4800-6. doi:10.1118/1.4736954.
- [30] Boers T, Brink W, Bianchi L, Saccomandi P, van Hespren J, Wennemars G, et al. An anthropomorphic thyroid phantom for ultrasound-guided radiofrequency ablation of nodules. 2023.
- [31] Lukas LA, Surry KJ, Peters TM. Temperature dosimetry using MR relaxation characteristics of poly(vinyl alcohol) cryogel (PVA-C). *Magn Reson Med*. 2001 Nov;46(5):1006-13. doi:10.1002/mrm.1288.
- [32] Adelnia H, Ensandoost R, Shebbrin Moonshi S, Gavvani JN, Vasafi EI, Ta HT. Freeze/thawed polyvinyl alcohol hydrogels: Present, past and future. *Eur Polym J*. 2022 Feb;164:110974. doi:10.1016/j.eurpolymj.2021.110974.
- [33] Surry KJM, Austin HJB, Fenster A, Peters TM. Poly(vinyl alcohol) cryogel phantoms for use in ultrasound and MR imaging. *Phys Med Biol*. 2004 Dec;49(24):5529. doi:10.1088/0031-9155/49/24/009.
- [34] Rossmann C, Haemmerich D. Review of temperature dependence of thermal properties, dielectric properties, and perfusion of biological tissues at hyperthermic and ablation temperatures. *Crit Rev Biomed Eng*. 2014;42(6):467. doi:10.1615/critrevbiomedeng.2015012486.

- [35] Chen SJS, Hellier P, Marchal M, Gauvrit JY, Carpentier R, Morandi X, et al. An anthropomorphic polyvinyl alcohol brain phantom based on Colin27 for use in multimodal imaging. *Med Phys.* 2012 Jan;39(1):554-61. doi:10.1118/1.3673069.
- [36] Wennemars G. Evaluating radiofrequency ablation on a thyroid phantom containing proteins using magnetic resonance imaging [Bachelor's thesis]. Enschede; 2022.
- [37] Saari RA, Nasri MS, Kida T, Yamaguchi M. Impact of Magnesium Salt on the Mechanical and Thermal Properties of Poly(vinyl alcohol). *Polymers.* 2021 Nov;13(21). doi:10.3390/polym13213760.
- [38] Nagura M, Hamano T, Ishikawa H. Structure of poly(vinyl alcohol) hydrogel prepared by repeated freezing and melting. *Polymer.* 1989 Apr;30(4):762-5. doi:10.1016/0032-3861(89)90169-9.
- [39] Yoshida A, Kato H, Kuroda M, Hanamoto K, Yoshimura K, Shibuya K, et al. Development of a phantom compatible for MRI and hyperthermia using carrageenan gel-relationship between T1 and T2 values and NaCl concentration. *Int J Hyperthermia.* 2004 Dec;20(8):803-14. doi:10.1080/0265673042000199268.
- [40] Mano I, Goshima H, Nambu M, Iio M. New polyvinyl alcohol gel material for MRI phantoms. *Magn Reson Med.* 1986 Dec;3(6):921-6. doi:10.1002/mrm.1910030612.
- [41] Murphy A. Factors affecting T1. *Radiopaedia.* 2020 Apr. doi:10.53347/rID-60741.
- [42] Luetkens JA, Voigt M, Faron A, Isaak A, Mesropyan N, Dabir D, et al. Influence of hydration status on cardiovascular magnetic resonance myocardial T1 and T2 relaxation time assessment: an intraindividual study in healthy subjects. *J Cardiovasc Magn Reson.* 2020 Dec;22(1):1-9. doi:10.1186/s12968-020-00661-9.
- [43] Brooks-Richards TL, Paxton NC, Allenby MC, Woodruff MA. Dissolvable 3D printed PVA moulds for melt electrowriting tubular scaffolds with patient-specific geometry. *Mater Des.* 2022 Mar;215:110466. doi:10.1016/j.matdes.2022.110466.
- [44] Wick-Joliat R, Tschamper M, Kontic R, Penner D. Water-soluble sacrificial 3D printed molds for fast prototyping in ceramic injection molding. *Addit Manuf.* 2021 Dec;48:102408. doi:10.1016/j.addma.2021.102408.
- [45] Goh WH, Hashimoto M. Fabrication of 3D Microfluidic Channels and In-Channel Features Using 3D Printed, Water-Soluble Sacrificial Mold. *Macromol Mater Eng.* 2018 Mar;303(3):1700484. doi:10.1002/mame.201700484.
- [46] Bauer BK, Meier C, Bietenbeck M, Lange PS, Eckardt L, Yilmaz A. Cardiovascular Magnetic Resonance-Guided Radiofrequency Ablation: Where Are We Now? *JACC: Clinical Electrophysiology.* 2022 Feb;8(2):261-74. doi:10.1016/j.jacep.2021.11.017.
- [47] Tarasek MR, Pellicer R, Hofstetter LW, Numan WCM, Bakker JF, Kotek G, et al. Validation of MR thermometry: Method for temperature probe sensor registration accuracy in head and neck phantoms. *Int J Hyperthermia.* 2014 Feb:142-9. Available from: <https://www.tandfonline.com/doi/full/10.3109/02656736.2014.887794>.
- [48] Winter L, Oberacker E, Paul K, Ji Y, Oezerdem C, Ghadjar P, et al. Magnetic resonance thermometry: Methodology, pitfalls and practical solutions. *Int J Hyperthermia.* 2015 Dec:63-75. doi:10.3109/02656736.2015.1108462.

**List of Tables**

1	Different settings of the radiofrequency catheter ablations on the heart phantom . . . . .	12
2	Settings for the different sequences to obtain $T_1$ maps. . . . .	12
3	Settings for the different sequences to obtain $T_2$ maps. . . . .	13

## List of Figures

1	Schematic visualisation of the heated volume. The volume affected by resistive heating is only a small part of the total damaged volume, mainly caused by conductive heating.[12][13] . . .	6
2	Schematic visualisation of the F-T process of a PVA solution. Starting with a solution containing PVA chains. Freezing this solution leads to the formation of ice crystals in between the PVA chains due to phase separation. Network junctions (circled in orange) will be formed during the thawing step. This establishes a gel network as the ice crystals become the pores of hydrogels.[32]	9
3	Design of the outer mold for the left ventricle, representing normal dimensions for healthy men. This mold is needed in duplicate to create the entire outer cast for the left ventricle. . . . .	11
4	Design of the inner mold for the left ventricle, representing normal dimensions for healthy men.	11
5	IR $T_1$ map of the phantom spheres. An increase in $T_1$ relaxation time can be observed, from approximately 1100 to 1350 ms, with increasing temperature (top left to bottom right column).	13
6	SE $T_2$ map of the phantom spheres. A slight increase in $T_2$ relaxation time can be observed from 230 to 280 ms with increasing temperature. At the last few spheres, the $T_2$ relaxation time decreases to 260 ms. . . . .	13
7	Calibration curve of the obtained $T_1$ relaxation times. This graph shows the change in $T_1$ relaxation time for the shown temperature range. The red dashed line shows the linear fit of the measurements including the equilibrium point at temperatures below 45°C. . . . .	14
8	Calibration curve of the obtained $T_2$ relaxation times. This graph shows the change in $T_2$ relaxation time for the shown temperature range. The red dashed line shows the linear fit of the measurements. . . . .	14
9	Calibration curve of the $T_1$ relaxation times of the 3 F-T cycle phantom spheres. The graph shows an increase in $T_1$ relaxation time in the temperature range of 44 to 62°C, with a starting point at 37°C and an end point at 70°C. The red dashed line shows the linear fit of the measurements including the equilibrium point at temperatures below 45°C. . . . .	14
10	Calibration curve of the $T_2$ relaxation times of the 3 F-T cycle phantom spheres. The graph shows the change in $T_2$ relaxation time in the temperature range of 44 to 62°C, with a starting point at 37°C and an ending point at 70°C. The red dashed line shows the linear fit of the measurements. . . . .	14
11	Calibration curves of the $T_1$ relaxation times of the PVA microtubes. The graph shows an increase in $T_1$ relaxation time in the temperature range of 44 to 70°C, with a starting point at 37°C. The dashed lines show the linear fits of the measurements including the equilibrium points at temperatures below 45°C. . . . .	15
12	Calibration curves of the $T_2$ relaxation times of the PVA microtubes. The graph shows the change in $T_2$ relaxation time in the temperature range of 44 to 70°C, with a starting point at 37°C. The dashed lines show the linear fit of the measurements. . . . .	15
13	Top view of the $T_1$ map after needle ablation, before applying erosion. . . . .	15
14	Top view of the $T_1$ map after needle ablation. Displayed is slice 21. All four ablated areas are slightly visible. The $T_1$ relaxation time increases from approximately 1300 to 1600 ms. . . . .	15
15	Front view of the $T_1$ map after needle ablation. Displayed is slice 15. Three of the ablated areas are visible with increased $T_1$ relaxation times. . . . .	16
16	Side view of the $T_1$ map after needle ablation. Displayed is slice 16. One ablated area is visible at the top, with an increased $T_1$ relaxation time. . . . .	16
17	Top view of the $T_2$ map after needle ablation. Displayed is slice 29. All of the four ablated areas are visible. The $T_2$ relaxation time increases from approximately 200 to 400 ms. . . . .	16
18	Front view of the $T_2$ map after needle ablation. Displayed is slice 22. All of the four ablated areas are visible with increased $T_2$ relaxation times. . . . .	16
19	Side view of the $T_2$ map after the needle ablation. Displayed is the central slice, slice 24. An ablated spot with a $T_2$ relaxation time of 410 ms can be seen in the top of the phantom. . . . .	16
20	Temperature map based on the $T_1$ linear fit. Displayed is slice 21. The temperature increases to 69.1°C in the most visible ablated spot. . . . .	17

---

21	Temperature map based on the $T_2$ linear fit. Displayed is slice 29. All of the ablated spots reach a temperature of $70^\circ\text{C}$ . . . . .	17
22	Front view of the $T_1$ map after RFA. Displayed is slice 35. . . . .	17
23	Top view of the $T_1$ map after RFA. . . . .	17
24	Front view of the $T_2$ map after RFA. Displayed is slice 35. One ablated spot is visible with a $T_2$ relaxation time of 1000 ms. . . . .	18
25	Top view of the $T_2$ map after RFA. The ablated spot has a $T_2$ relaxation time of 250 ms. . . . .	18
26	Front view of the temperature map based on the $T_1$ calibration curve. Displayed is slice 35. . . . .	18
27	Top view of the temperature map based on the $T_1$ calibration curve. . . . .	18
28	3D rendering of the $T_1$ temperature map. The lesion is clearly visible with a temperature of $>70^\circ\text{C}$ , according to the linear fitted model. . . . .	18
29	Front view of the temperature map based on the $T_2$ calibration curve. Displayed is slice 35. . . . .	19
30	Top view of the temperature map based on the $T_2$ calibration curve. . . . .	19
31	Signal intensity curve of a random pixel. . . . .	21
32	Signal intensity curve of the pixel with the highest $T_1$ relaxation time. . . . .	21